



The participation of ilmenite-bearing cumulates in lunar mantle overturn

Y. Zhao^{a,*}, J. de Vries^{a,b}, A.P. van den Berg^{a,b}, M.H.G. Jacobs^c, W. van Westrenen^a

^a Faculty of Science, Vrije Universiteit Amsterdam, the Netherlands

^b Dept. Earth Sciences, Utrecht University, the Netherlands

^c Institute of Metallurgy, Clausthal University of Technology, Germany

ARTICLE INFO

Article history:

Received 25 November 2017

Received in revised form 19 November 2018

Accepted 10 January 2019

Available online 1 February 2019

Editor: B. Buffett

Keywords:

Moon

mantle overturn

thermal evolution

geodynamical modelling

ilmenite-bearing cumulates

ABSTRACT

The ilmenite-bearing cumulates (IBC) formed from the solidification of the lunar magma ocean are thought to have significantly affected the long-term evolution of the lunar interior and surface. Their high density is considered to trigger Rayleigh–Taylor instabilities which allow them to sink into the solidified cumulates below and drive a large-scale overturn in the lunar mantle. Knowledge of how the IBC participate in the overturn is important for studying the early lunar dynamo, chemistry of surface volcanism, and the existence of present-day partial melt at the lunar core–mantle boundary. Despite early efforts to study this process as Rayleigh–Taylor instabilities, no dynamical models have quantified the degree of IBC sinking systematically. We have performed quantitative 2-D geodynamical simulations to measure the extent to which IBC participate in the overturn after their solidification, and tested the effect of a range of physical and chemical parameters. Our results show that IBC overturn most likely happened when the magma ocean had not yet fully solidified, with the residual melt decoupling the crust and IBC, resulting in 50–70% IBC sinking. Participation of the last dregs of remaining magma ocean melt is unlikely, leaving its high concentrations of radiogenic elements close to the surface. Our simulations further indicate that foundered IBC can stay relatively stable at the core–mantle boundary until the present day, at temperatures consistent with the presence of a partially molten zone in the deep mantle as inferred from geophysical data. 30–50% of the primary IBC remain at shallow depths throughout lunar history, enabling their assimilation by rising magma to form high-Ti basalts.

© 2019 The Authors. Published by Elsevier B.V. This is an open access article under the CC BY-NC-ND license (<http://creativecommons.org/licenses/by-nc-nd/4.0/>).

1. Introduction

The Moon is considered to have solidified from a global magma ocean (Dowty et al., 1974; Warren, 1985). The solidification process produced a radial gradient of compositions due to fractional crystallization. In the late stages of lunar magma ocean (LMO) crystallization (Lin et al., 2017; Snyder et al., 1992; Warren, 1985), denser cumulates containing ilmenite, known as the ilmenite-bearing cumulates (IBC), are formed. The last part of the magma ocean to solidify is the so-called urKREEP (potassium, rare earth elements, and phosphorus-rich silicate liquid), just below the newly-formed flotation crust. This layer is highly enriched in incompatible elements, including radiogenic isotopes of Th, U and K. The presence of dense IBC at shallow depths in the Moon results in gravitational instability, leading to a mantle overturn event, where dense cumulates sink down into the earlier-formed cumulates (Hess and

Parmentier, 1995; Parmentier et al., 2002; Ringwood and Kesson, 1976). In this study, we provide new constraints on the extent of participation of IBC in lunar mantle overturn.

The fate of the IBC and the overlying urKREEP layer exerts major influence on global lunar evolution. Firstly, if the IBC sank to the core–mantle boundary, they would have significant influence on the ancient lunar dynamo (Cournède et al., 2012; Hood, 2011; Tikoo et al., 2017) through their impact on the thermal evolution of the core (Zhang et al., 2013). Secondly, the mantle overturn is thought to have played a key role in the formation of the mare basalts exposed at the lunar surface, with IBC being the most likely source of the high Ti content of high-Ti basalts. Thirdly, present-day IBC at the core–mantle boundary could explain the presence of partial melt in the deep mantle. Multiple lines of geophysical evidence (Garcia et al., 2011; Khan et al., 2004, 2014, and references therein; Weber et al., 2011) suggest the presence of a deep melt layer in the lunar interior today. Part of this melt layer is likely located in the deep lunar mantle, in a layer ~150 km thick with 5–30% melt (Weber et al., 2011). Foundered IBC may have persisted at the core–mantle boundary in a partially molten state

* Corresponding author.

E-mail address: y.zhao@vu.nl (Y. Zhao).

until the present day (Dyger et al., 2016; van Kan Parker et al., 2012; Zhang et al., 2017), explaining geophysical observations.

Solid state convection would occur irrespective of whether or not IBC were able to participate in it. Therefore, the problem of “mantle overturn” is twofold. Firstly, it concerns when the first overturn, which marks the onset of solid-state convection, would happen: during or after the solidification of the magma ocean. Secondly, it concerns whether or not, and to which extent, IBC would participate in any part of the solid-state convection. The first issue was addressed recently by Maurice et al. (2017) and Boukaré et al. (2018). They found that the onset of solid-state convection may have occurred before the IBC were solidified, depending on the competition of time scales between solidification and convective overturn, and on the viscosity of the cumulate layer. Taken at face value, the age of the Moon (at least ~ 4.51 Ga, Barboni et al., 2017) and the observed age of the lunar crust (~ 4.36 Ga, e.g. Borg et al., 2011) imply a possible LMO solidification time of ~ 150 – 200 Myr. However, estimates of the time scale of magma ocean solidification range from ten or a few tens of Myr (Elkins-Tanton et al., 2011) to 100–200 Myr (Hess and Parmentier, 1995; Solomon and Longhi, 1977). The discrepancy between the low estimates and observation may be resolved by considering tidal heating of the crust (Elkins-Tanton et al., 2011). $\sim 80\%$ of the LMO is thought to have solidified on a short time scale of ~ 1000 yr (Elkins-Tanton et al., 2011), before an insulating flotation crust was formed. Due to its lower effective Rayleigh number, the lunar interior is expected to be mixed to a smaller extent than the Earth, Mars, and Venus before full solidification of the magma ocean (Maurice et al., 2017).

In view of the importance of the evolution of IBC, our study focuses on the second issue. Many previous studies have shed light on the evolution of IBC, although no systematic assessments have quantified the degree of IBC sinking. Hess and Parmentier (1995, 2001) studied how multiple stages of convective mixing during and after LMO solidification can explain the source of early magmatism and Mg-suite formation, and create a thicker and diluted IBC layer through sinking of early IBC diapirs as IBC solidify. The thickness of the IBC layer is a key parameter used in determining the wavelength of IBC downwelling (Parmentier et al., 2002). de Vries et al. (2010) decoupled the crust and the IBC by using a constant low-viscosity layer below the crust, thereby making all of the IBC sink. While investigating the fashion in which previously overturned IBC-rich materials rise back up, Zhang et al. (2013) assumed the foundered IBC-rich materials at the core–mantle boundary contain 30% of IBC, after mixing with the olivine-rich mantle.

Here, we aim to assess, through geodynamic modelling, whether or not and to what extent IBC would participate in mantle convection. Instead of terming the event of interest “mantle overturn”, we refer to it as “IBC overturn”, to emphasize the fact that we specifically investigate the fate of IBC after they have solidified, irrespective of whether the earlier cumulates below have already undergone convective overturn events. In particular, we quantify the percentage of IBC that sinks into the mantle (referred to as IBC% in the rest of the paper) and impacts the thermal evolution of the deep lunar interior, and test the effects of a range of physical and chemical parameters in our convection models. We investigate whether or not urKREEP is still in a partially molten state at the onset of IBC overturn and explore the implications of our results for lunar evolution.

2. Modelling approach

Since it is uncertain when the IBC overturn occurs, we test two scenarios. In the first, we assume that IBC overturn starts after the LMO has entirely solidified. The initial temperature profile used for these models, especially in the region of the IBC layer, has a particularly large influence on early model evolution, due to the

temperature dependence of viscosity. This set of models therefore tests the effect of initial temperature, and temperature dependence of viscosity, on IBC overturn behaviour. In the second scenario, we assume that the LMO has not entirely solidified at the time of IBC overturn. urKREEP is highly enriched in radiogenic isotopes of Th, U and K (Warren, 1985). It also has relatively low melting temperatures (Lin et al., 2017). Therefore it may have been kept in a high-melt-fraction state by its own heat production, even after the rest of the magma ocean solidified (Hess and Parmentier, 2001; Solomon and Longhi, 1977). Such a partially molten layer is weak, and may have acted as a decoupling agent that facilitates IBC overturn. Therefore in the second class of models, we consider that IBC transport begins just after the ilmenite-bearing layer is solidified, and before the urKREEP layer is entirely solidified. In this case, we test the effect of urKREEP layer weakening, the density contrast between IBC and the layer below, the thickness of the IBC layer, and the distribution of urKREEP heat-producing elements between the crust and IBC.

2.1. Description of the numerical model

Modelling experiments are performed on a 2-dimensional cylindrical finite element mesh with an aperture angle of 180° . Convection equations are solved using the extended Boussinesq approximation (Christensen and Yuen, 1985), including viscous dissipation and adiabatic heating, assuming the incompressible fluid has an infinite Prandtl number.

Model equations for thermal convection in a highly viscous fluid are based on the conservation of energy, momentum, and mass. Non-dimensionalisation of the convection equations is done by using the thickness of the mantle h as the spatial scale, the thermal diffusion time h^2/κ_0 as timescale, where $\kappa_0 = 9 \times 10^{-7} \text{ m}^2 \text{ s}^{-1}$ is the thermal diffusivity scale. Dimensional temperature is written as $T = T_s + T'\Delta T$, where T_s is the surface temperature and ΔT is the initial temperature difference over the depth of the domain. In the remainder of this paper, the accent of non-dimensional variables is dropped in the notation.

The energy equation

$$\frac{DT}{Dt} = \alpha g(r) Di(T + T_0)w + \frac{Di}{Ra} \Phi + \partial_j(\kappa \partial_j T) + R_H H(\vec{C}, t) \quad (1)$$

describes the rate of temperature change by the four terms on the right hand side: adiabatic heating, viscous dissipation, heat conduction, and heat production from radiogenic sources, respectively. $D \cdot /Dt$ is the Lagrangian derivative. Parameters in this and the following equations are explained in Table 1. The momentum equation

$$\partial_j(\eta(P, T)e_{ij}) - \partial_i \Delta P = g(r)\hat{e}_{ri} B(T, \vec{C}) Ra \quad (2)$$

describes the force balance of viscous shear, dynamic pressure gradient, and buoyancy. \hat{e}_{ri} is a unit vector in the direction of gravity. $B(T, \vec{C}) = (\rho(T, \vec{C}) - \rho_0)/(\rho_0 \alpha_0 \Delta T)$ is the buoyancy factor. The conservation of mass

$$\partial_j v_j = 0 \quad (3)$$

is described as a divergence-free velocity field for incompressible fluid.

Composition is modelled by 500,000 active tracers, advected by the flow and using the particle-in-cell method (Hockney and Eastwood, 1988). Particle transport is described by the non-diffusive transport equation

$$\frac{D\vec{C}}{Dt} = 0. \quad (4)$$

Table 1
Meanings and values of the parameters used in model equations.

Parameter	Meaning	Value
C	Composition parameter	
c_p	Specific heat	1250 J kg ⁻¹ K ⁻¹
c_{pc}	Specific heat of the core	800 J kg ⁻¹ K ⁻¹
Di	Dissipation number $Di = \frac{\alpha_0 g_0 h}{c_p}$	0.0719
e_{ij}	Strain rate tensor: $e_{ij} = \frac{\partial u_i}{\partial x_j} + \frac{\partial u_j}{\partial x_i}$	
e	Second invariant of the strain rate: $\sqrt{\frac{1}{2} e_{ij} e_{ij}}$	
g	Gravitational acceleration	
g_0	Gravity scale value/surface gravity	1.62 m s ⁻²
$H(\vec{C}, t)$	Composition and time dependent internal heat production	
h	Domain height (thickness of mantle)	1387 km
$k(P, T)$	Thermal conductivity	
L	Thickness of hot layer in Scenario B models	10, 15, or 20 km
σ	Viscosity contrast created by hot layer in Scenario B models	0.1 or 0.01
$q_c(t)$	Average heat flow through core–mantle boundary	
r	Radial coordinate	
R_H	Internal heating number: $R_H = \frac{H_0 h^2}{c_p \kappa_0 \Delta T}$	
Ra	Thermal Rayleigh number: $Ra = \frac{\rho_0 \alpha_0 g_0 \Delta T h^3}{\eta_0 \kappa_0}$	10 ⁶
ΔT	Temperature scale value	1650 K
T_s	Surface temperature	250 K
T_0	Dimensionless surface temperature $T_0 = \frac{T_s}{\Delta T}$.	
T_c	Core temperature	
T_p	Potential temperature of an adiabat	
t	Time	
V_c	Core volume	1.8×10^8 km ³
v_i	Cartesian component of the velocity field	
w	Radial velocity	
α_0	Thermal expansion scale value	4×10^{-5} K ⁻¹
η_0	Viscosity scale value (reference viscosity)	1×10^{21} Pa s
κ	Thermal diffusivity: $\kappa = \frac{k}{\rho c_p}$	
ρ_0	Density scale value	3354 kg m ⁻³
ρ_c	Core density	7400 kg m ⁻³
Φ	Viscous dissipation: $\Phi = \eta e^2$	

The components C_i of the composition vector \vec{C} represent the mass fractions of the material components (mineral associations) and $C_{N_c} = 1 - \sum_{j=1}^{N_c-1} C_j$. N_c is the number of components of the composition. Applying linearized thermal expansion and assuming a single uniform thermal expansivity α for all components, the effective density is given as $\frac{1}{\rho(\vec{C}, T)} = \sum_{i=1}^{N_c} \frac{C_i}{\rho_{ir}(1 - \alpha(T - T_s))}$, where ρ_{ir} is the density of component i at reference temperature T_s (Table 2).

Our numerical experiments are performed using a finite element code based on the SEPRAN finite element package (Segal and Praagman, 2000; van den Berg et al., 2015). Quadratic triangular elements are used in this study. The finite element mesh has 28784 elements. The element size is gradually reduced to 5 km towards the top and bottom of the mantle. Several tests with increased resolution of the finite element mesh, and increased number of active tracers, reproduced our model results.

2.2. Parameter overview and choices

A list of model parameters is presented in Table 1. Temperature- and pressure-dependent variable thermal conductivity $k(P, T)$ (van den Berg et al., 2005) is used, calculated from Hofmeister's (1999) conductivity model for average mantle materials based on phonon solid state physics.

The 40 km-thick lunar crust (within the range of 34–43 km derived from lunar gravity field observations, Wiczeorek et al., 2013) is assumed to have a uniform thermal conductivity of $k_{crust} = 1 \text{ W m}^{-1} \text{ K}^{-1}$. This is calculated based on the contributions to the overall crustal thermal resistance of the bulk crust and near-surface porous layers. Temperature- and pressure-dependent viscosity is modelled based on the Arrhenius relation:

$$\eta(P, T) = \eta_{pre} \exp\left(\frac{E^* + PV^*}{RT}\right) \quad (5)$$

E^* is the activation energy which determines temperature dependence. $V^* = 6 \text{ cm}^3 \text{ mol}^{-1}$ (Karato and Wu, 1993) is the activation volume controlling pressure dependence. $R = 8.314 \text{ kg m}^2 \text{ s}^{-2} \text{ K}^{-1} \text{ mol}^{-1}$ is the gas constant, and T is absolute temperature. The viscosity scale η_0 is 1×10^{21} Pa s in all models, resulting in a thermal Rayleigh number of $Ra = 1 \times 10^6$. η_{pre} is the viscosity pre-factor, such that at a depth of 500 km and temperature of 1500 K, $\eta(P, T) = 1 \times 10^{20}$ Pa s. Two viscosity truncation values are applied to avoid numerical instability: 1×10^{18} Pa s at the lower end, and 1×10^{24} Pa s at the higher end.

Gravity decreases from 1.62 m s^{-2} at the surface to 0.52 m s^{-2} at the core–mantle boundary, similar to that in the VPREMOON model (Garcia et al., 2011). The thermal expansivity α has a surface value of $4 \times 10^{-5} \text{ K}^{-1}$ and decreases to $3.24 \times 10^{-5} \text{ K}^{-1}$ at the bottom of the mantle. Core radius is 350 km, an intermediate value from a range of estimations (Khan et al., 2007; Williams et al., 2001; Weber et al., 2011; Shimizu et al., 2013).

2.3. Boundary conditions and thermal coupling of mantle and core

Mechanical boundary conditions are no slip on the surface and free slip along all other boundaries. The surface of the Moon is given a constant temperature of 250 K. The core is modelled as a finite heat reservoir, the cooling of which is controlled by heat flux across the core–mantle boundary (van den Berg et al., 2005). The initial temperature of the core is set at 1900 K, corresponding to the peridotite solidus temperature (Hirschmann, 2000) at core–mantle boundary pressure conditions. Temperature evolution of the core is described by equation (6) below, where $A = 7.7 \times 10^5 \text{ km}^2$ is the surface area at the core–mantle bound-

Table 2

Density values used in each initial material component layer. These values are calculated from Snyder et al. (1992, his Fig. 4) for 1 bar and 250 K. The reference density value used in the models is 3354 kg m⁻³. Layer# is as indicated in the left frame of Fig. 1.

Layer#	Layer composition	Density (kg m ⁻³)
I	100% Plagioclase	2750
II	24.8% Ilmenite80 ((Mg _{0.2} Fe _{0.8})TiO ₃) + 75.2% Clinopyroxene	3719
III	75% Clinopyroxene + 25% Olivine	3396
IV	100% Orthopyroxene	3324
V	100% Olivine	3342

ary and $q_c(t)$ is time-dependent heat flow across the core–mantle boundary.

$$\frac{dT_c}{dt} = -\frac{A}{\rho_c c_p V_c} q_c(t) \quad (6)$$

2.4. Initial model setup

The initial conditions of our models are based on the LMO fractional crystallization sequence of Snyder et al. (1992) (Fig. 1, left). The stratified result of crystallisation is modelled by prescribing density and distribution of heat-producing elements corresponding to the different layers. Density values of each layer are presented in Table 2. They are calculated for the corresponding layer compositions derived from Snyder et al. (1992, their Fig. 4) at 1 bar and 250 K.

Heat-producing isotopes ²³⁵U, ²³⁸U, ²³²Th and ⁴⁰K are used as heat sources (de Vries, 2012, her Table 5.4), calculated from mineral–melt partition parameters of each element assuming an initial bulk lunar heat production of 5.2×10^{-12} W kg⁻¹. For a mixture of material components, heat production is described by:

$$H(\vec{C}, t) = \sum_{i=1}^{N_c} C_i H_i(t), \quad H_i(t) = \sum_{j=1}^{N_{iso}} H_{ij} \exp(-\lambda_j t) \quad (7)$$

where C_i is the mass fraction of material component i , $H_i(t)$ is the instantaneous heat productivity of component i . H_{ij} is the initial heat productivity of isotope j in material component i . λ_j is related to the half-life of isotope j .

Due to its low thickness, the urKREEP layer is not resolved as a separate initial layer and material component. Its highly concentrated heat-producing element inventory is assumed to be incorporated in either the IBC below or the crust above (Section 2.4.2).

To investigate whether IBC overturn happens with or without solidification of urKREEP at the onset of IBC overturn, two scenarios of initial mantle temperature conditions are used in our models. Both scenarios (described in sections 2.4.1 and 2.4.2 below) use horizontally averaged depth-dependent temperature profiles. Details of all models are presented in Table 3 and summarised below.

2.4.1. Scenario A: IBC overturn in entirely solidified magma ocean

For the first scenario we assume that the IBC overturn event started directly after the magma ocean entirely solidified. These models are relevant when considering the possible short time scale of lunar crustal formation (Elkins-Tanton et al., 2011; Perera et al., 2018). The initial temperature profile is defined as an adiabatic profile truncated at the thermal boundary layers. Both the core–mantle boundary and surface thermal boundary layers are 40 km thick. A series of adiabats are calculated based on lunar parameters using potential temperatures of 1200 to 1800 K, at 100 K intervals. Example initial T profiles are shown in the middle frame of Fig. 1.

Experimental results of Karato and Wu (1993) indicate an activation energy E^* of 300 kJ mol⁻¹ for dry olivine in diffusion creep. We investigated the effects of contrasting values of 300 and 100 kJ mol⁻¹ for E^* . The latter value approximates the effect of

power-law rheology (Christensen, 1984). Activation volume is kept constant at $V^* = 6$ cm³ mol⁻¹ (Karato and Wu, 1993).

2.4.2. Scenario B: IBC overturn with partially molten urKREEP

To investigate the impact of mechanical decoupling of the IBC layer on its convective overturn, a second scenario is investigated where the urKREEP layer is still in a partially molten state. To simulate the correspondingly low viscosity of partially molten urKREEP as a transient phenomenon, a hot layer is prescribed in the initial temperature profile, resulting in a local weak zone. The initial temperature profile is composed of the peridotite solidus (Hirschmann, 2000) and an adiabat with a potential temperature of 1640 K. Fig. 1(right) illustrates two of these initial temperature profiles (solid green and red lines). All Scenario B models assume an activation energy of $E^* = 300$ kJ mol⁻¹ (Table 3). The initial viscosity profiles of our models differ only by their corresponding initial temperature profiles. Representative initial viscosity profiles from this work are shown together with profiles from previous studies in Fig. 2. As in most previous studies, our models do not explicitly consider compositional dependence of viscosity, although recent experimental measurements of the rheological properties of ilmenite indicate the IBC have a lower viscosity than other LMO cumulate layers (Dyger et al., 2016). When compositional effects are not considered, numerical models overestimate the viscosity of IBC by at least one order of magnitude (Fig. 2).

A local and transient hot layer in Scenario B models lowers the viscosity of the IBC region, and the goal of this thermal anomaly is to mimic the effects of the presence of partial melt in the urKREEP layer. The effect of this hot layer only exists at the beginning of the model evolution (Section 3.2.1), and it is not meant to explicitly simulate the compositional effect of ilmenite on IBC viscosity. Since the effect of the presence of weak urKREEP is also to lower the viscosity of the IBC region, it has a similar role in facilitating IBC overturn to the role of compositional effects of ilmenite (Dyger et al., 2016), partial melt, and/or water in the IBC region.

Two parameters are varied for the hot layer: layer thickness L and viscosity contrast σ such that σ is multiplied by the original viscosity. $\eta(P, T) = \sigma \eta_{org}(P, T)$. This is achieved by raising the temperature of the layer by around 150 K for $\sigma = 0.1$ and around 330 K for $\sigma = 0.01$ (Fig. 1, right, upper inset). When the hot layer is 10 km thick, there are 2–3 elements (5–7 nodal points) in the hot layer. In particular, model ScenB_15_1e-2_1deltarho is used as a reference model for subsequent testing of other parameters (Table 3).

We also assess the effect of IBC density contrast. Contrasts tested are 0, $0.5\delta\rho$, $\delta\rho$, $1.5\delta\rho$, and $2\delta\rho$, where $\delta\rho = (3719 - 3396)$ kg/m³ = 323 kg/m³ (Table 2). This is equivalent to setting the ilmenite content of the IBC to 0, 5.5%, 11%, 16.5%, and 22%, respectively, or to varying the Mg# of an IBC layer with 11% ilmenite from 75 to 80. The initial temperature of model ScenB_15_1e-2_1deltarho_30km (right frame of Fig. 1, solid green line) is used in all these models.

Hess and Parmentier (1995) envisioned that, for a magma ocean that solidified in ~ 200 Myr, diapirs of first crystallized IBC would sink 80 km, producing a total, less dense IBC layer of 100 km thick before driving a larger overturn. Models ScenB_15_1e-2_1deltarho_

Table 3
All models in this study and their key parameters.

Model name	Initial T	Initial T details	Partially molten urKREEP	Activation energy (kJ/mol)	Density contrast (kg/m^3)	IBC layer thickness (km)	Heat production of urKREEP	
ScenA_PT1200_E100	Adiabats with various T_p	$T_p = 1200$	No	100	323	30	in IBC	
ScenA_PT1300_E100		$T_p = 1300$						
ScenA_PT1400_E100		$T_p = 1400$						
ScenA_PT1500_E100		$T_p = 1500$						
ScenA_PT1600_E100		$T_p = 1600$						
ScenA_PT1700_E100		$T_p = 1700$						
ScenA_PT1700_E100		$T_p = 1800$						
ScenA_PT1200_E300		$T_p = 1200$		300				
ScenA_PT1300_E300		$T_p = 1300$						
ScenA_PT1400_E300		$T_p = 1400$						
ScenA_PT1500_E300		$T_p = 1500$						
ScenA_PT1600_E300		$T_p = 1600$						
ScenA_PT1700_E300		$T_p = 1700$						
ScenA_PT1700_E300		$T_p = 1800$						
ScenB_10_1e-1_1deltarho_30km	Adiabats with $T_p = 1640$ K + solidus	$L = 10$ km, $\sigma = 0.1$	yes	300	323	30	in IBC	
ScenB_15_1e-1_1deltarho_30km		$L = 15$ km, $\sigma = 0.1$						
ScenB_20_1e-1_1deltarho_30km		$L = 20$ km, $\sigma = 0.1$						
ScenB_10_1e-2_1deltarho_30km		$L = 10$ km, $\sigma = 0.01$						
ScenB_15_1e-2_1deltarho_30km		$L = 15$ km, $\sigma = 0.01$						
ScenB_20_1e-2_1deltarho_30km		$L = 20$ km, $\sigma = 0.01$						
ScenB_15_1e-2_0deltarho_30km		$L = 15$ km, $\sigma = 0.01$						
ScenB_15_1e-2_0.5deltarho_30km								0
ScenB_15_1e-2_1.5deltarho_30km								161.5
ScenB_15_1e-2_2deltarho_30km								484.5
ScenB_15_1e-2_1deltarho_50km								646
ScenB_15_1e-2_1deltarho_100km								323
ScenB_15_1e-2_1deltarho_30km_crust								30

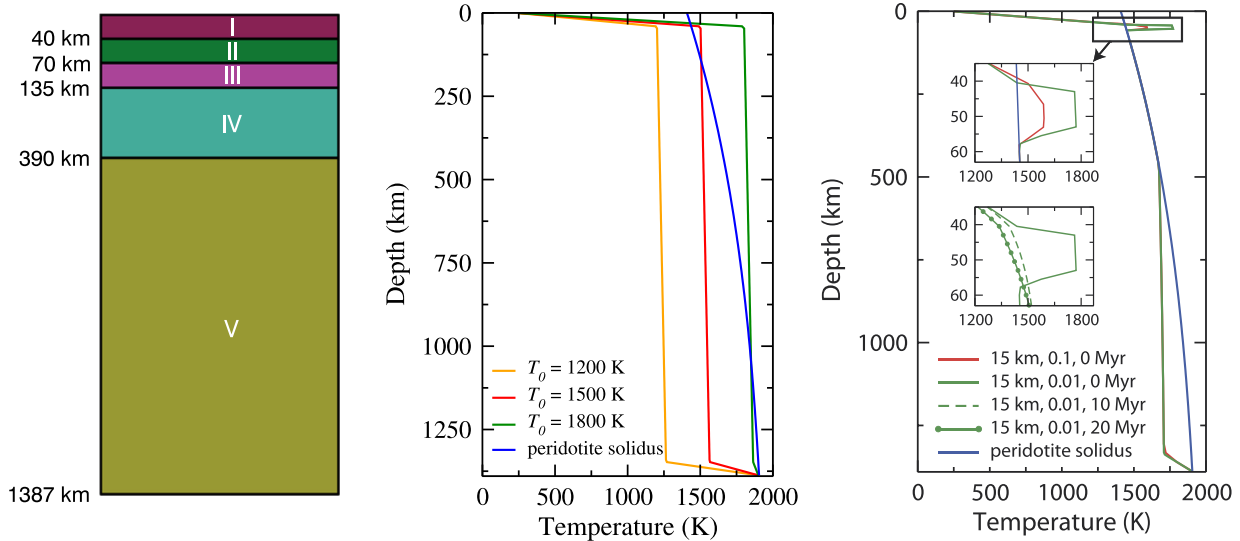


Fig. 1. Left: initial configuration of the material composition of all models (for details see Table 2). Middle: Scenario A initial temperature profiles using adiabats of varying potential temperatures. Right: Scenario B initial temperatures of $L = 15$ km, $\alpha = 0.1$ and 0.01 . Note that the two profiles of different viscosity contrasts differ only at 40–65 km depth. Below the hot layer, the initial temperatures are composed of the peridotite solidus, and an adiabat with $T_p = 1640$ K. The lower inset is time evolution of profile with $L = 15$ km and $\alpha = 0.01$, showing the transient nature of the hot layer. (For interpretation of the colours in the figure(s), the reader is referred to the web version of this article.)

50km and ScenB_15_1e-2_1deltarho_100km (Table 3) test the effects of such a “diluted” IBC layer of 50 km and 100 km thickness, respectively. The extra mass and heat production of the original IBC layer is homogeneously and volumetrically redistributed in the corresponding thicker layers.

For all models described above we assume that all radiogenic elements of the urKREEP layer follow the IBC. If instead they become part of the crust, heat loss from the surface would tend to be faster, and the IBC would benefit less from a high heating rate. The effect of the distribution of heat production is tested by comparing the model in which the urKREEP layer heat production is entirely uniformly distributed in the IBC (model

ScenB_15_1e-2_1deltarho_30km) with a model where heat production remains in the crust (model ScenB_15_1e-2_1deltarho_30km_crust). Model ScenB_15_1e-2_1deltarho_30km_crust uses the same initial temperature and density contrast ($\delta\rho = 323$ kg/m^3) as model ScenB_15_1e-2_1deltarho_30km (Table 3).

3. Results

Figs. 3 and 4 give selected snapshots of modelling results from the reference model ScenB_15_1e-2_1deltarho_30km of Scenario B. Fig. 3 shows 2-D snapshots of composition, at various stages of the IBC overturn. The left column highlights the evolution of IBC.

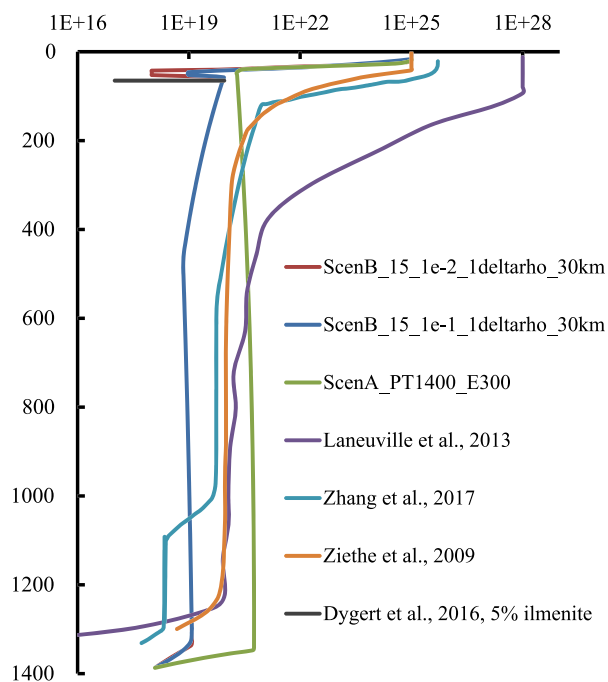


Fig. 2. Representative initial viscosity profiles used in this study, compared to previous numerical models (Laneuville et al., 2013; Zhang et al., 2013; Ziethe et al., 2009) and recent experimental results (Dygert et al., 2016). Model descriptions of this study can be found in Table 3. The viscosity range from Dygert et al. (2016) corresponds to the viscosity range of 5% ilmenite content at 1200 °C for the isostress and Tullis model (see their Fig. 4).

The colour scale shows the concentration of materials coming from the original IBC layer in the initial condition. The middle and right columns show mass concentrations of materials from the two layers originally below IBC (Fig. 1, left). For clarity, only one material component is shown in each plot. At 6 Myr after the start of the models, IBC diapirs have started to reach the deeper mantle. After 100 Myr, a layer of IBC have settled at the bottom of the mantle.

Fig. 4 shows the vertical distribution of IBC fractional content calculated from the type of snapshots shown in Fig. 3. The content value is cumulative, from the surface down to the core–mantle boundary. As the overturn progresses, more IBC content moves to deeper regions. Just underneath the crust, there is a fast increase of IBC content with depth. As the IBC diapirs sink into the mantle, the heat in the partially molten urKREEP dissipates away, and the thickness of the surface thermal boundary layer (lithosphere) increases. At 8 Myr, for example, this rate of increase has a clear change at ~ 100 km depth, which marks the lower boundary of the lithosphere. Within a few hundred Myr, the amount of IBC that stay within the lithosphere reaches a steady level. This marks the end of the sinking of IBC (last row of Fig. 3). In the case of model ScenB_15_1e-2_1deltarho_30km, about 32% of the IBC remain at shallow depth. This value does not change in the next hundreds of million years but slightly increases by a few percent at billion-year scale as the lithosphere thickens and catches more IBC to be “frozen” into it.

In the remainder of this paper, results are presented in terms of the percentage of IBC that participate in the overturn (“IBC%”) as a function of various parameters. This IBC% is calculated at the depth of maximum curvature in plots such as those shown in Fig. 4. This is where the rate of increase of IBC content with depth has the sharpest change, implying the lower boundary of the lithosphere. The precise depth at which this value occurs differs from model to model, but it is roughly 100 km below surface.

3.1. Scenario A: IBC overturn when magma ocean is fully solidified

Results of this set of models are summarized in Fig. 5a. The horizontal axis corresponds to the potential temperatures of the adiabatic initial temperature profiles (Section 2.4.1). When $E^* = 300 \text{ kJ mol}^{-1}$ is used in the Arrhenius viscosity model, IBC% is 0 for potential temperatures T_p lower than 1300 K. At T_p of 1400 K, 1500 K and 1600 K, IBC % increases rapidly from 14% to 55% and to 79%, respectively. When $E^* = 100 \text{ kJ mol}^{-1}$, the temperature dependence of viscosity is low, viscosity calculated from Equation (6) is lower, and IBC% is higher. Although IBC% is 0 at $T_p = 1000$ K, it increases to 38% and 57% at $T_p = 1100$ K and $T_p = 1200$ K.

3.2. Scenario B: IBC overturn when urKREEP is still partially molten

3.2.1. Effect of urKREEP layer weakening

Fig. 5b shows results of Scenario B models with a partially molten urKREEP layer (Section 2.4.2). IBC% increases with both layer thickness and layer viscosity contrast, due to the lowered local viscosity in the partially molten layer. For all parameter combinations that simulate the urKREEP layer, IBC% ranges from 51 to 74. Without the hot layers simulating urKREEP, the initial temperature used in Scenario B models is around 1450 K at the depths of the IBC, comparable to model ScenA_PT1400_E300 whose IBC% is less than 20. When the effect of a weak urKREEP layer is simulated, IBC% more than doubles.

Our results show that the local thermal anomaly in the hot layer disappears from the temperature field within the first 10 Myr as its heat dissipates away (Fig. 1, right plot, lower inset). The overturn timescale (Fig. 4) is an order of magnitude higher. This means that even if the partial melt in urKREEP was present in only the beginning of the overturn process, within 10 Myr after the solidification of IBC, it would have played a key role in facilitating mantle overturn.

3.2.2. Effect of density contrast of the IBC layer

Results of varying the IBC density contrasts, applied to the reference model ScenB_15_1e-2_1deltarho_30km, are shown in Fig. 5c. IBC% range from 49 to 77. As expected, higher density in the IBC results in higher IBC%. The effect of $\delta\rho$ decreases with increasing $\delta\rho$. Between density contrast of 0 and $2\delta\rho$, IBC% can have a difference of 28. This is an effect similar in magnitude to that of the urKREEP parameters in Section 3.2.1.

3.2.3. Effect of IBC layer thickness

Results of Models ScenB_15_1e-2_1deltarho_50km and ScenB_15_1e-2_1deltarho_100km are shown in Fig. 5d. IBC% increases with IBC thickness from 70% at 50 km to 82% at 100 km. Even though density contrast decreases with IBC thickness, IBC sinking is still mildly facilitated by layer thickness due to the greater depths to which IBC are distributed.

3.2.4. Effect of radiogenic heat distribution

Our models show that the extent to which urKREEP, with its high abundance of radiogenic heat-producing elements, is assumed to be incorporated into IBC during IBC sinking does not have much effect on the amount of IBC sinking. There is only 5% difference in IBC sinking percentage between adding all heating in the urKREEP layer to the IBC layer (Fig. 5b), as in model ScenB_15_1e-2_1deltarho_30km (IBC% = 71) and leaving all this heating in the crust (model ScenB_15_1e-2_1deltarho_30km_crust, IBC% = 66).

3.2.5. Effect of variable thermal conductivity

When model ScenB_15_1e-2_1deltarho_30km is run with a uniform thermal conductivity $k = 4 \text{ W m}^{-1} \text{ K}^{-1}$ in the mantle and

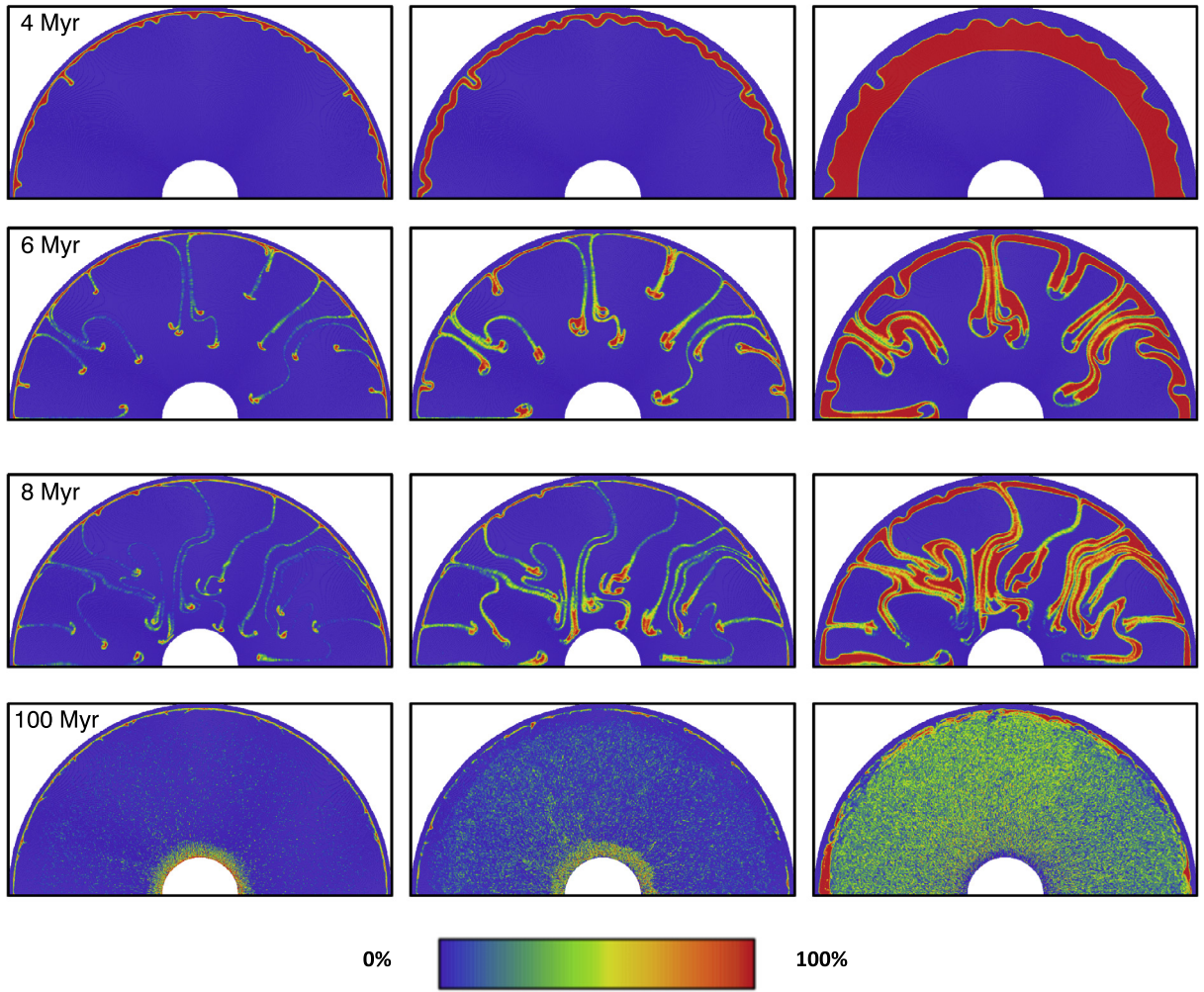


Fig. 3. Left: concentration of material from the original IBC layer in model ScenB_15_1e-2_1deltarho_30km. Middle and right: concentration of material from the two layers, III and IV defined in Table 2, originally below IBC in model ScenB_15_1e-2_1deltarho_30km.

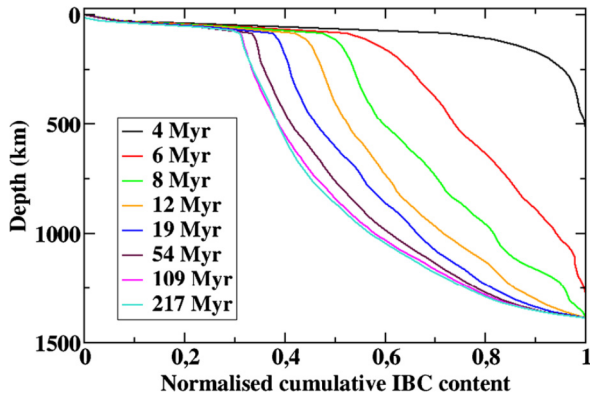


Fig. 4. Evolution of normalised vertical distribution of IBC in model ScenB_15_1e-2_1deltarho_30km.

the crust, it gives an IBC% of 16, far less than the 71 predicted by model ScenB_15_1e-2_1deltarho_30km. When a uniform $k_{crust} = 4 \text{ W m}^{-1} \text{ K}^{-1}$ is used with a variable $k_{mantle}(P, T)$, IBC% = 22, showing that most of the insulating effects come from the crust. Plagioclase, combined with the porous megaregolith and regolith layers in the crust, modelled by a crustal conductivity $k_{crust} = 1 \text{ W m}^{-1} \text{ K}^{-1}$, promotes the sinking of IBC by delaying conductive cooling and growth of the lithosphere.

3.3. Present-day melt percentage in deep mantle

To investigate possible long-term consequences of IBC overturn, we extended models ScenB_15_1e-2_1deltarho_30km and ScenB_15_1e-2_1deltarho_30km_crust (Section 3.2.4) so that their thermo-chemical evolution can be tracked up to the present day. In our view these two models have initial parameters most representative for early lunar conditions. They use $E^* = 300 \text{ kJ mol}^{-1}$ in their viscosity, and a density contrast of $\delta\rho = 323 \text{ kg m}^{-3}$, corresponding to 11% ilmenite content close to the likely ilmenite content of the IBC on the basis of LMO crystallization models (Snyder et al., 1992; Lin et al., 2017). They also represent two end-member cases, where either all of urKREEP heat production follows IBC (ScenB_15_1e-2_1deltarho_30km) or all of urKREEP stays with the crust (ScenB_15_1e-2_1deltarho_30km_crust).

Present-day temperatures of both models are below the peridotite solidus, but to assess whether these models can yield areas of partial melting at present, solidi of individual cumulates must be considered. Here we only consider the melting of ilmenite-bearing materials, which yield the lowest melting temperatures in the lunar mantle. Using the 2-D temperature fields of these two models, we assess present-day melting in the deep lunar mantle by comparing them to the solidus and liquidus of ilmenite-bearing materials measured experimentally at 2–4.7 GPa (Wyatt, 1977). Wyatt's results do not cover pressures below 2 GPa, but they are suitable for our analysis of melting behaviour in the deep man-

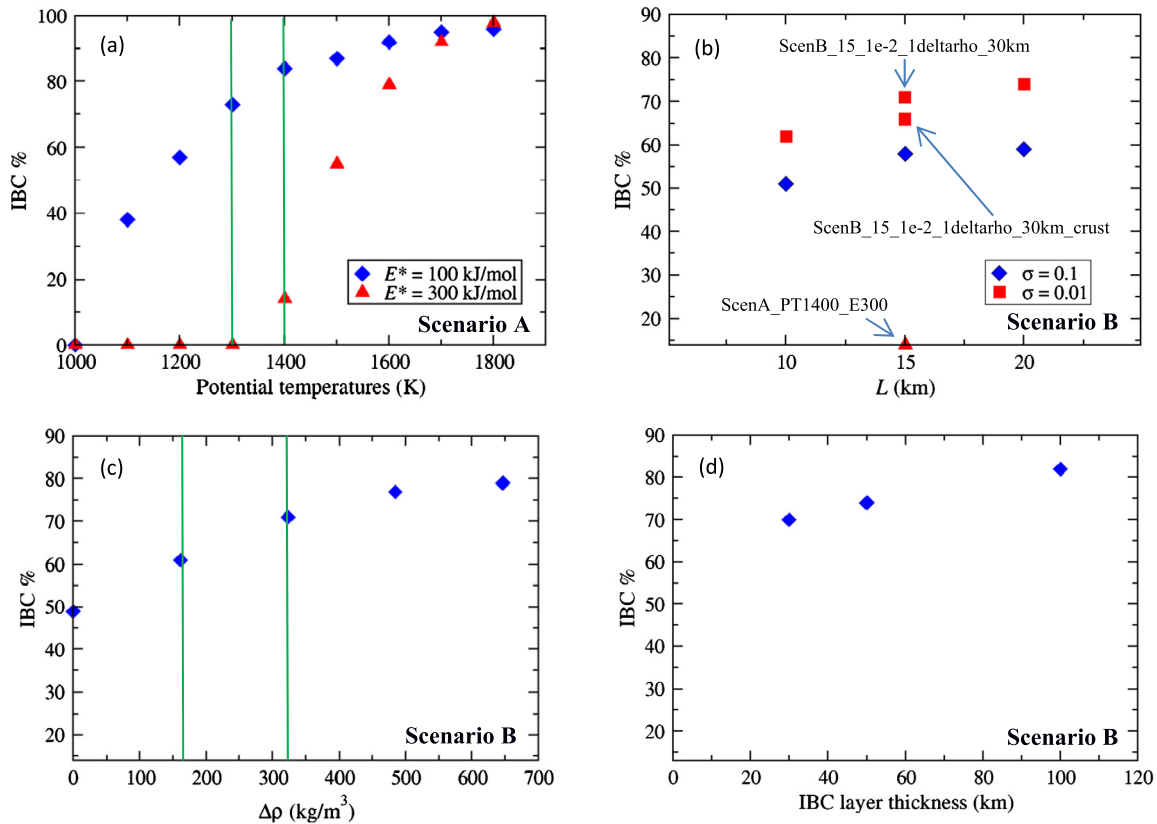


Fig. 5. Summary of results. Panel (a) presents results of Scenario A models, whereas panels (b), (c) and (d) show those of Scenario B models. Results in (b) demonstrate the effect of urKREEP layer weakening and thickness. Those in (c) show effects of density contrast. (d) shows effects of IBC layer thickness. Models in (c) and (d) use $L = 15$ km and $\sigma = 0.01$. $\delta\rho$ is 323 kg/m^3 in all models except when $\delta\rho$ is tested in (c) models. IBC layer thickness is 30 km except when it is tested in (d) models. Green lines in (a) indicate the initial temperatures most relevant to the early Moon, based on the solidi of peridotite and IBC (Lin et al., 2017). Green lines in (c) indicate density contrasts most relevant to the Moon. The upper boundary corresponds to the density contrast derived from experimental results (Lin et al., 2017). The lower boundary corresponds to a “diluted” IBC layer of 100 km, assuming early IBC cumulates sink to a distance of 80 km during the full solidification of IBC (Hess and Parmentier, 1995).

tle as that is the region where partial melt may be present in the Moon today (e.g. Weber et al., 2011; van Kan Parker et al., 2012). At 4.7 GPa, the solidus is 1470°C , while the liquidus is 1620°C . Both the solidus and liquidus increase with increasing pressure with a slope of 60°C/GPa . A linear increase of melt percentage is assumed at temperatures between solidus and liquidus. Melt percentages are scaled by the concentration of IBC in the local environment, so that, for example, in an area containing 40% IBC at a temperature halfway between the solidus and liquidus of the corresponding pressure, the melt percentage of the local region is assumed to be 20%.

Results are displayed in Fig. 6. From the melt percentage plots (middle and lower rows), we can see that model ScenB_15_1e-2_1deltarho_30km predicts a present-day partially molten region in the bottom 30–50 km of the mantle. Model ScenB_15_1e-2_1deltarho_30km_crust, on the other hand, predicts a ~ 150 km thick partially molten layer above the core–mantle boundary. This region has a volumetric average of $\sim 25\%$ melt.

4. Discussion

Our results show that IBC% is strongly influenced by a range of physical parameters, and also the relative timescales of processes. If IBC overturn occurred after the entire solidification of the magma ocean, the lithosphere grows rapidly, IBC tend to be “frozen” in the highly viscous lithosphere before sufficient time has elapsed to start the sinking. This is only likely when the magma ocean solidified within 10 Myr, which corresponds to the lower bound of current estimates (Elkins-Tanton et al., 2011;

Perera et al., 2018). This short timeframe is an order of magnitude lower than the difference, albeit debated, between the age of the Moon (at least ~ 4.51 Ga, Barboni et al., 2017) and the observed age of the lunar crust (~ 4.36 Ga, e.g. Borg et al., 2011). On the other hand, if the urKREEP layer stays in a high-melt-percentage state long enough, it would facilitate IBC overturn. Recent rheological measurements (Dyger et al., 2017) indicate low viscosity of relevant magma ocean melt, suggesting that younger portions of the crust segregated efficiently out of the liquid. Together with the plausible long timescale of LMO solidification (Solomon and Longhi, 1977; Hess and Parmentier, 1995), this makes it likely that the low viscosity of partially molten urKREEP facilitated IBC sinking.

Based on our results, the most important factors governing the extent of the participation of IBC in overturn are urKREEP layer weakening, low thermal conductivity of the crust, initial temperatures in the region of the IBC, and the temperature dependence of viscosity. All of these factors boil down to the viscosity in the vicinity of the IBC layer.

4.1. IBC overturn at full solidification of the magma ocean

Models starting with an entirely solidified magma ocean show that IBC tend not to participate in overturn, using $E^* = 300 \text{ kJmol}^{-1}$. According to Lin et al. (2017), IBC are formed at 0.4 GPa, when 90% of the magma ocean has solidified. At such pressure conditions, the solidus of peridotite is around 1460 K (Hirschmann, 2000). The solidus of IBC is less than 100 K lower than that of peridotite at the depth of the IBC layer (Lin et al.,

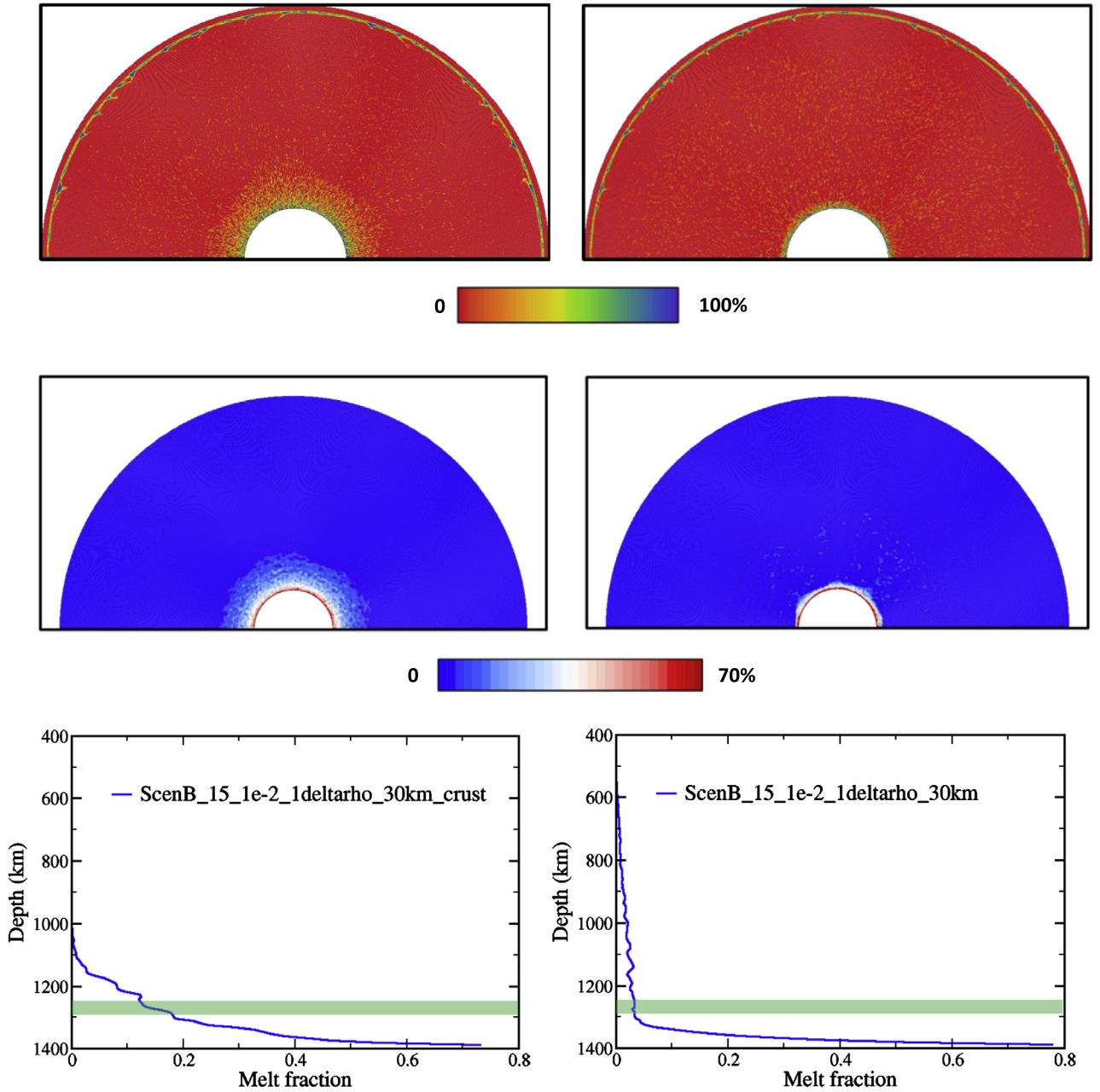


Fig. 6. Top: snapshots of IBC concentration at 4.5 Gyr, representing the present day. Middle: corresponding melt percentages at 4.5 Gyr. Bottom: horizontal averages of melt percentages showing the vertical distributions of present-day melt. The green bands show the depth of the partial melt boundary estimated by Weber et al. (2011). Left: model ScenB_15_1e-2_1deltarho_30km_crust. Right: ScenB_15_1e-2_1deltarho_30km.

2017). These solidus temperatures are comparable to an adiabat with a potential temperature of 1400 K at IBC depth. This means that, to model solidified IBC, initial temperatures cannot exceed the adiabat of potential temperature 1400 K. Based on our results in Section 3.1 (Fig. 5a), when the experimentally determined activation energy of 300 kJ mol^{-1} is used, less than 20% IBC would participate in convective overturn. Only Newtonian rheology is considered in our models. Christensen (1984) suggested that power-law rheology can be approximated by a reduced activation energy in Newtonian rheology. This implies that power-law rheology can potentially lower local viscosity and facilitate IBC sinking. Our results indicate that when power-law rheology is approximated by assuming a lower $E^* = 100 \text{ kJ mol}^{-1}$, IBC% is higher than 80%, more than 4 times higher than that assuming Newtonian rheology at $E^* = 300 \text{ kJ mol}^{-1}$.

4.2. IBC overturn with partially molten magma ocean residue

When a partially molten urKREEP layer is modelled, and when only considering parameter values that lie within a realistic range, IBC% vary between 50 and 70. It is important to note that the amount of IBC sinking is never 100%; some of the IBC always remain at shallow levels. The detailed parameterization of the partially molten urKREEP layer includes the thickness of the urKREEP layer and the viscosity of the material, the latter representing factors such as the degree of melting. These factors involve many uncertainties, which influence IBC% to a moderate extent. Density contrast was tested over a wide range, representing from 0 to 22% ilmenite in IBC, or a Mg# of 75–80 with 11% ilmenite content. When density contrasts are low, an increase of the modal abundance of ilmenite by 5% results in an increase of IBC% by $\sim 10\%$. When ilmenite content is higher than 11%, the effect of

density contrast is smaller, due to other stronger factors such as the growth of the lithosphere. The effect of any realistic density contrast on IBC% is less than 20%. The viscosity contrast and thickness of the partially molten urKREEP, and the density contrast, are secondary factors that influence IBC overturn. When the IBC layer thickness is higher due to the growth of sinking diapirs during the solidification of IBC, further sinking is facilitated due to the redistribution of IBC to greater, thus warmer and less viscous, depths. This process increases IBC% by $\sim 10\%$. The distribution of urKREEP heat-producing elements between the crust and the IBC has little effect on IBC%.

Dygert et al.'s rheological experiments (2016) show that ilmenite has an effective viscosity at least three orders of magnitude lower than that of olivine, and thereby weakens the dense ilmenite-bearing cumulates, facilitating sinking. Lin et al.'s (2017) experiments show that the IBC contain about 15% ilmenite. This means that the IBC would have at least one order of magnitude lower viscosity than the harzburgitic lunar mantle (Dygert et al., 2016). This effect may reach 3 orders of magnitude in the isostress mixing model, even for 5% ilmenite content. Such a low IBC viscosity would result in higher IBC%, similar to the effect of the partially molten urKREEP layer. On the other hand, the peridotite solidus is used in our Scenario B initial temperatures. Since the IBC have a solidus within 100 K lower at its original depth, sub-solidus evolution of the IBC may have started at a lower temperature. This would decrease IBC sinking by roughly 10%.

4.3. Long-term consequences of IBC overturn

4.3.1. Distribution of urKREEP heat production and the present-day partially molten zone above the lunar core

Model ScenB_15_1e-2_1deltarho_30km_crust is arguably the model closest to reality. Since urKREEP has a low solidus and contains high quantities of heat-producing elements, it was very likely in a partially molten state when IBC solidified. As long as urKREEP remains at low viscosity for a few Myr after solidification of IBC, it would strongly facilitate IBC overturn. Since the IBC are only likely to sink in large quantities when the urKREEP is still partially molten and buoyant, the proportion of urKREEP heat-producing elements that IBC can carry down is likely not high. Indeed, our model assuming urKREEP heat production staying under the crust (model ScenB_15_1e-2_1deltarho_30km_crust) predicts present-day partial melt in the lunar lower mantle that is in better agreement with geophysical observations than the model assuming urKREEP heat production sinking with IBC (model ScenB_15_1e-2_1deltarho_30km). Therefore urKREEP was likely partially molten during IBC overturn, and mostly remained at shallow depths. Even though in model ScenB_15_1e-2_1deltarho_30km, slightly more IBC sink into the mantle due to additional heat production in the IBC layer, it predicts less partial melt from foundered IBC and a smaller partially molten region in the present day. The reason can be found in the IBC concentration plots (upper row of Fig. 6). The additional heat production in the foundered IBC helps them to stay thermally buoyant enough to participate in convection, instead of forming a stable layer at the core–mantle boundary. If the present-day partial melt in the lunar deeper mantle is indeed due to the foundered IBC from LMO cumulates, it would imply that solid-state convection started before the LMO was entirely solidified. This may help constrain the duration of LMO solidification (Maurice et al., 2017; Boukaré et al., 2018). It would also mean that most of the urKREEP likely stayed in the lithosphere.

4.3.2. Present-day distribution of ilmenite-rich compositions and its implications

Based on our model results, present-day IBC are partially locked up in the lithosphere and partially form a stable layer above the core–mantle boundary. Model ScenB_15_1e-2_1deltarho_30km_crust concurs with Zhang et al. (2017) in that foundered IBC tend to stay at the bottom of the mantle throughout lunar evolution. This means that it is hard to explain the chemistry of near-side volcanism by a deep rising plume from the lower mantle that carries up foundered IBC. Our Model ScenB_15_1e-2_1deltarho_30km_crust disagrees with Stegman and Richards (2003) model TB-2, where foundered IBC rise up in a secondary overturn, driving an episode of lunar dynamo. This disagreement is mainly due to the low density contrast used in Stegman et al.'s model. In all our models, small pockets of IBC are still left close to their original shallow formation depth, even when most of the IBC sink down. These reservoirs vary in size depending on the percentage of IBC that remain in the lithosphere. This means that any rising partial melt from below the lithosphere has the possibility to assimilate ilmenite-rich materials left behind by IBC overturn, consistent with an assimilation scenario for the formation of high-titanium magmas (Hubbard and Minear, 1975; Wagner and Grove, 1997; Elkins-Tanton et al., 2002; Dygert et al., 2013).

A stable layer of IBC at the core–mantle boundary inhibits heat extraction from the outer core through a blanketing effect. Without IBC rising back up, the lunar dynamo cannot be explained by the secondary overturn that brings cold materials down.

4.4. Wavelength of sinking IBC diapirs

When IBC layer thickness is kept at 30 km, our models show IBC overturn at wavelengths of ~ 400 km. This wavelength is increased to >600 km when IBC layer thickness is 100 km. This is consistent with the stability analysis of Parmentier et al. (2002), which showed that wavelength of the fastest-growing IBC diapirs increases with layer thickness and viscosity contrast. Parmentier et al. (2002) observed a degree-one downwelling when the IBC have a viscosity four orders of magnitude lower than that of the layer below. This level of viscosity contrast may be achieved when considering the combined effect of the low viscosity of IBC and partial melt and/or presence of water (Dygert et al., 2016).

5. Conclusions and implications

Participation of ilmenite-bearing cumulates (IBC) in mantle overturn is highly sensitive to their viscosity and the viscosity of the surrounding layers. Parameters that have a first-order influence on IBC sinking are initial temperature in the region of IBC and the temperature dependence of viscosity, the presence of a partially molten urKREEP layer, and an insulating crust with low thermal conductivity. Second-order influences come from the thickness and degree of melting of the partially molten urKREEP, density contrast between IBC and the layer below, and IBC layer thickness. IBC overturn most likely happened when the urKREEP layer was still partially molten, with 50–70% of the original IBC layer sinking down. Participation of urKREEP in IBC sinking is unlikely. Some of the IBC would always remain at shallow levels, making it possible for rising partial melt to assimilate the Ti-rich composition. Foundered IBC would likely form a stable layer at the core–mantle boundary. This could explain the presence of present-day partially molten lower lunar mantle, but complicates explanations for the generation and maintenance of the lunar dynamo.

Acknowledgements

We wish to thank Nick Dygert for his thoughtful comments and suggestions which significantly improved this manuscript. This work is made possible through the financial support by the Netherlands Organisation for Scientific Research (N.W.O.) Vici grant awarded to WwW (grant number 865.13.006). We also thank T. van Zessen (Utrecht University) for his technical assistance with the computer cluster.

References

- Barboni, M., Boehnke, P., Keller, B., Kohl, I.E., Schoene, B., Young, E.D., Mckeegan, K.D., 2017. Early formation of the Moon 4.51 billion years ago. *Sci. Adv.* 3, e1602365. <https://doi.org/10.1126/sciadv.1602365>.
- Borg, L.E., Connelly, J.N., Boyet, M., Carlson, R.W., 2011. Chronological evidence that the Moon is either young or did not have a global magma ocean. *Nature* 477, 70–72. <https://doi.org/10.1038/nature10328>.
- Boukaré, C.-E., Parmentier, E.M., Parman, S.W., 2018. Timing of mantle overturn during magma ocean solidification. *Earth Planet. Sci. Lett.* 491, 216–225. <https://doi.org/10.1016/j.epsl.2018.03.037>.
- Christensen, U., 1984. Convection with pressure- and temperature-dependent non-Newtonian rheology. *Geophys. J. R. Astron. Soc.* 77, 343–384.
- Christensen, U.R., Yuen, D.A., 1985. Layered convection induced by phase transitions. *J. Geophys. Res.* 90 (B12), 10291–10300. <https://doi.org/10.1029/JB090iB12p10291>.
- Cournède, C., Gattacceca, J., Rochette, P., 2012. Magnetic study of large Apollo samples: possible evidence for an ancient centered dipolar field on the Moon. *Earth Planet. Sci. Lett.* 331–332, 31–42. <https://doi.org/10.1016/j.epsl.2012.03.004>.
- de Vries, J., 2012. Lunar Evolution: A Combined Numerical Modelling and HPT Experimental Study. PhD Diss., Utrecht University, Chapter 5. <https://dspace.library.uu.nl/handle/1874/237788>.
- de Vries, J., van den Berg, A.P., van Westrenen, W., 2010. Formation and evolution of a lunar core from ilmenite-rich magma ocean cumulates. *Earth Planet. Sci. Lett.* 292 (1–2), 139–147. <https://doi.org/10.1016/j.epsl.2010.01.029>.
- Dowty, E., Prinz, M., Keil, K., 1974. Ferroan anorthosite: a widespread and distinctive lunar rock type. *Earth Planet. Sci. Lett.* 24, 15–25.
- Dygert, N., Liang, Y., Hess, P., 2013. The importance of melt TiO₂ in affecting major and trace element partitioning between Fe–Ti oxides and lunar picritic glass melts. *Geochim. Cosmochim. Acta* 106, 134–151. <https://doi.org/10.1016/j.gca.2012.12.005>.
- Dygert, N., Hirth, G., Liang, Y., 2016. A flow law for ilmenite in dislocation creep: implications for lunar cumulate mantle overturn. *Geophys. Res. Lett.* 43, 532–540. <https://doi.org/10.1002/2015GL066546>.
- Dygert, N., Lin, J.-F., Marshall, E.W., Kono, Y., Gardner, J.E., 2017. A low viscosity lunar magma ocean forms a stratified anorthitic flotation crust with mafic poor and rich units. *Geophys. Res. Lett.* 44. <https://doi.org/10.1002/2017GL075703>.
- Elkins-Tanton, L.T., Van Orman, J.A., Hager, B.H., Grove, T.L., 2002. Re-examination of the lunar magma ocean cumulate overturn hypothesis: melting or mixing is required. *Earth Planet. Sci. Lett.* 196, 239–249.
- Elkins-Tanton, L.T., Burgess, S., Yin, Q.-Z., 2011. The lunar magma ocean: reconciling the solidification process with lunar petrology and geochronology. *Earth Planet. Sci. Lett.* 304, 326–336. <https://doi.org/10.1016/j.epsl.2011.02.004>.
- Garcia, R.F., Gagnepain-Beyneix, J., Chevrot, S., Lognonné, P., 2011. Very preliminary reference Moon model. *Phys. Earth Planet. Inter.* 188 (1–2), 96–113. <https://doi.org/10.1016/j.pepi.2011.06.015>.
- Hess, P.C., Parmentier, E.M., 1995. A model for the thermal and chemical evolution of the Moon's interior: implications for the onset of mare volcanism. *Earth Planet. Sci. Lett.* 134, 501–514.
- Hess, P.C., Parmentier, E.M., 2001. Thermal evolution of a thicker KREEP liquid layer. *J. Geophys. Res.* 106, 28023–28032. <https://doi.org/10.1029/2000JE001416>.
- Hirschmann, M.M., 2000. Mantle solidus: experimental constraints and the effects of peridotite composition. *Geochem. Geophys. Geosyst.* 1, 1042. <https://doi.org/10.1029/2000GC000070>.
- Hockney, R., Eastwood, J., 1988. *Computer Simulations Using Particles*. Institute of Physics Publishing Ltd., Bristol.
- Hofmeister, A.M., 1999. Mantle values of thermal conductivity and the geotherm from phonon lifetimes. *Science* 283 (5408), 1699–1706. <https://doi.org/10.1126/science.283.5408.1699>.
- Hood, L.L., 2011. Central magnetic anomalies of Nectarian-aged lunar impact basins: probable evidence for an early core dynamo. *Icarus* 211 (2), 1109–1128. <https://doi.org/10.1016/j.icarus.2010.08.012>.
- Hubbard, N.J., Minear, J.W., 1975. A physical and chemical model of early lunar history. In: *Proceedings of the 6th Lunar Science Conference*, pp. 1057–1085.
- Karato, S., Wu, P., 1993. Rheology of the upper mantle: a synthesis. *Science* 260 (5109), 771–778. <https://doi.org/10.1126/science.260.5109.771>.
- Khan, A., Mosegaard, K., Williams, J.G., Lognonné, P., 2004. Does the Moon possess a molten core? Probing the deep lunar interior using results from LLR and Lunar Prospector. *J. Geophys. Res.* 109, E09007. <https://doi.org/10.1029/2004JE002294>.
- Khan, A., Connolly, J., MacLennan, J., Mosegaard, K., 2007. Joint inversion of seismic and gravity data for lunar composition and thermal state. *Geophys. J. Int.* 168, 243–258.
- Khan, A., Connolly, J.A.D., Pommier, A., Noir, J., 2014. Geophysical evidence for melt in the deep lunar interior and implications for lunar evolution. *J. Geophys. Res., Planets* 119, 2197–2221. <https://doi.org/10.1002/2014JE004661>.
- Laneuville, M., Wiczorek, M.A., Breuer, D., Tosi, N., 2013. Asymmetric thermal evolution of the Moon. *J. Geophys. Res.* 118, 1435–1452.
- Lin, Y., Tronche, E.J., Steenstra, E.S., van Westrenen, W., 2017. Evidence for an early wet Moon from experimental crystallization of the lunar magma ocean. *Nat. Geosci.* 10, 14–18.
- Maurice, M., Tosi, N., Samuel, H., Plesa, A.-C., Hüttig, C., Breuer, D., 2017. Onset of solid-state mantle convection and mixing during magma ocean solidification. *J. Geophys. Res., Planets* 122, 577–598. <https://doi.org/10.1002/2016JE005250>.
- Parmentier, E.M., Zhong, S., Zuber, M.T., 2002. Gravitational differentiation due to initial chemical stratification: origin of lunar asymmetry by the creep of dense KREEP? *Earth Planet. Sci. Lett.* 201, 473–480.
- Perera, V., Jackson, A.P., Elkins-Tanton, L.T., Asphaug, E., 2018. Effect of re-impacting debris on the solidification of the lunar magma ocean. *J. Geophys. Res., Planets*. <https://doi.org/10.1029/2017JE005512>.
- Ringwood, A.E., Kesson, S.E., 1976. A dynamic model for mare basalt petrogenesis. In: *Proc. 7th Lunar Sci. Conf.*, vol. 2, pp. 1697–1722.
- Segal, A., Praagman, N.P., 2000. The SEPRAN Package. Technical Report. <http://ta.twi.tudelft.nl/sepran/sepran.html>. (Accessed 26 November 2017).
- Shimizu, H., Matsushima, M., Takahashi, F., Shibuya, H., Tsunakawa, H., 2013. Constraint on the lunar core size from electromagnetic sounding based on magnetic field observations by an orbiting satellite. *Icarus* 222 (1), 32–43. <https://doi.org/10.1016/j.icarus.2012.10.029>.
- Snyder, G.A., Taylor, L.A., Neal, C.R., 1992. A chemical model for generating the sources of mare basalts: combined equilibrium and fractional crystallization of the lunar magmasphere. *Geochim. Cosmochim. Acta* 56, 3809–3823.
- Solomon, S.C., Longhi, J., 1977. Magma oceanography 1: thermal evolution. In: *Proc. Lunar Sci. Conf.*, vol. 8, pp. 583–599.
- Stegman, D.R., Richards, M.A., 2003. An early lunar core dynamo driven by thermochemical mantle convection. *Nature* 421, 143–146.
- Tikoo, S.M., Weiss, B.P., Shuster, D.L., Suavet, C., Wang, H., Grove, T.L., 2017. A two-billion-year history for the lunar dynamo. *Sci. Adv.* 3. <https://doi.org/10.1126/sciadv.1700207>.
- van den Berg, A.P., Rainey, E., Yuen, D., 2005. The combined influences of variable thermal conductivity, temperature- and pressure-dependent viscosity and core-mantle coupling on thermal evolution. *Phys. Earth Planet. Inter.* 149, 259–278.
- van den Berg, A.P., Segal, G., Yuen, D.A., 2015. SEPRAN: a versatile finite-element package for a wide variety of problems in geosciences. *J. Earth Sci.* 26 (1), 89–95. <https://doi.org/10.1007/s12583-015-0508-0>.
- van Kan Parker, M., Sanloup, C., Sator, N., Guillot, B., Tronche, E.J., Perrillat, J.-P., Mezouar, M., Rai, N., van Westrenen, W., 2012. Neutral buoyancy of titanium-rich melts in the deep lunar interior. *Nat. Geosci.* 5 (3), 186–189. <https://doi.org/10.1038/ngeo1402>.
- Wagner, T.P., Grove, T.L., 1997. Experimental constraints on the origin of lunar high-Ti ultramafic glasses. *Geochim. Cosmochim. Acta* 61 (6), 1315–1327. [https://doi.org/10.1016/S0016-7037\(96\)00387-0](https://doi.org/10.1016/S0016-7037(96)00387-0).
- Warren, P.H., 1985. The magma ocean concept and lunar evolution. *Annu. Rev. Earth Planet. Sci.* 13, 201–240.
- Weber, R.C., Lin, P., Garnero, E.J., Williams, Q., Lognonné, P., 2011. Seismic detection of the lunar core. *Science* 331, 309–312.
- Wiczorek, M.A., et al., 2013. *Science* 339, 671–675.
- Williams, J., Boggs, D., Yoder, C., Ratcliff, J., Dickey, J., 2001. Lunar rotational dissipation in solid body and molten core. *J. Geophys. Res.* E 11, 27933–27968.
- Wyatt, B.A., 1977. The melting and crystallisation behaviour of a natural clinopyroxene-ilmenite intergrowth. *Contrib. Mineral. Petrol.* 61, 1. <https://doi.org/10.1007/BF00375941>.
- Zhang, N., Parmentier, E.M., Liang, Y., 2013. A 3-D numerical study of the thermal evolution of the Moon after cumulate mantle overturn: the importance of rheology and core solidification. *J. Geophys. Res., Planets* 118, 1789–1804. <https://doi.org/10.1002/jgre.20121>.
- Zhang, N., Dygert, N., Liang, Y., Parmentier, E.M., 2017. The effect of ilmenite viscosity on the dynamics and evolution of an overturned lunar cumulate mantle. *Geophys. Res. Lett.* 44. <https://doi.org/10.1002/2017GL073702>.
- Ziethé, R., Seiferlin, K., Hiesinger, H., 2009. Duration and extent of lunar volcanism: comparison of 3D convection models to mare basalt ages. *Planet. Space Sci.* 57, 784–796.